

OPTICAL ANGULAR MANIPULATION OF LIQUID CRYSTAL DROPLETS IN LASER TWEEZERS

E. BRASSELET*

*Centre de Physique Moléculaire Optique et Hertzienne,
Université Bordeaux 1, CNRS, 351 Cours de la Libération,
33405 Talence Cedex, France
e.brasselet@cpmoh.u-bordeaux1.fr

S. JUODKAZIS

*Research Institute for Electronic Science,
Hokkaido University, N21W10 CRIS Bldg.,
Sapporo 001-0021, Japan*

Received 8 May 2009

The high sensitivity of liquid crystals to external fields, especially electromagnetic fields, confer to them fascinating properties. In the case of light fields, their large optical nonlinearities over a broad spectrum have great application potential for all-optical devices. The linear optical properties of liquid crystals, such as their high refractive index, birefringence and transparency, are also of great practical interest in optofluidics, which combines the use of optical tools in microfluidic environments. A representative example is the laser micromanipulation of liquid crystalline systems using optical tweezing techniques. Liquid crystal droplets represent a class of systems that can be easily prepared and manipulated by light, with or without a nonlinear light-matter coupling. Here we review different aspects of quasi-statics and dynamical optical angular manipulation of liquid crystal droplets trapped in laser tweezers. In particular, we discuss to the influence of the phase (nematic, cholesteric or smectic), the bulk ordering symmetry, the droplet size, the polarization state and power of the trapping light, together with the prominent role of light-matter angular momentum exchanges and optical orientational nonlinearities.

Keywords: Liquid crystal droplets; laser tweezers; optical orientational nonlinearities; light-matter angular momentum transfer.

1. Introduction

Since the pioneering work of Ashkin almost four decades ago,¹ laser tweezers have found many applications in noncontact easy handling and characterization of matter at the micron scale, as summarized in many reviews on optical tweezing.^{2–6} Besides

*Corresponding author.

the possible optical manipulation in the three dimensions, angular manipulation at a fixed location is another extensively exploited characteristic of laser tweezers, that basically involves a coupling between the trapping light field and the trapped object. This has been originally demonstrated by Friese *et al.*⁷ by using transparent birefringent calcite microcrystals. In their experiment, the trapped microcrystals were realigned and rotated by light owing to spin angular momentum (i.e., the angular momentum associated with the polarization state) transfer. This opened the way toward the realization of optically driven micromachines controlled by spatiotemporal light beam shaping using holographic optical tweezers, fast electro-optic polarization switching or methods relying on interference patterns. Solid state architectures may also be fabricated, but the use of *in situ* reconfigurable micro-optical elements is desirable, for which liquid crystals (LCs) are good candidates. The main reasons are the various existing ordered phases (the most common being the nematic, cholesteric and smectic phases⁸), the high sensitivity of their orientational order to external fields (e.g. thermal, mechanical, chemical, electric, magnetic or electromagnetic), and their high birefringence over a very broad range of electromagnetic frequencies. Among the different uses of LCs in laser trapping experiments, one can distinguish the following practical situations, where LCs (i) represent the surrounding medium of a trapped microparticle, (ii) play simultaneously the role of the host fluid and of the trapped object, and (iii) constitute the trapped object itself, which is immersed in an isotropic host medium.

The first case corresponds to colloidal particles immersed in LCs — as proposed by Poulain *et al.*⁹ — where the orientational distortions induced by the particles are associated with a structural force field. One can mention the experiment of Muševič *et al.*,¹⁰ where particles having a refractive index lower than the surrounding LCs can be trapped and manipulated owing to surface-induced and laser-induced distortions around the particle. Later, such nonintuitive behaviors have been demonstrated to be a general feature of laser trapping in anisotropic fluids where polarization of light plays a crucial role.¹¹ The optical tweezing of single microparticles hosted in an anisotropic fluid can also be used for material structuration (such as the controlled generation and manipulation of defects¹²) and characterization (such as the measurement of the anisotropic hydrodynamics properties of LCs¹³ or of the anisotropic force field of a LC colloid itself¹⁴).

In the second case, these are the LC defects or structures that are directly manipulated by light. Demonstrations have been done in nematic,¹⁵ smectic¹⁶ and cholesteric^{17,18} mesophases, with application to the determination of *in situ* material properties without the need for a perturbing guest particle as a probe such as the line tension of disclination lines.¹⁷ Conversely, light-induced structural deformations can also be used to manipulate LC localized structures.¹⁸

The last case mainly refers LC droplets dispersed in an immiscible host fluid (e.g. water). Then, interfacial tension brings a droplet into almost perfectly spherical shape whose size can be precisely controlled.^{19,20} LC droplets are easily trapped

and manipulated by light, due to their high refractive index and birefringence. Actually, reliable light-controlled displacement and/or angular optical manipulation have been demonstrated in various mesophases, such as nematic,^{21–23} smectic²⁴ or cholesteric LCs.^{13,25} Although the most intuitive way to achieve light-induced rotation of LC droplets is to operate a spin angular momentum transfer similarly to the seminal experiment of Friese *et al.*,⁷ light scattering and/or photon absorption processes may also be considered.²³ Importantly, the large optical orientational nonlinearities of LCs^{26,27} can also come into play and enrich much the optical angular manipulation strategies, as demonstrated experimentally in pure LC droplets^{25,29,30} and theoretically predicted in the presence of particular photoinduced effects.³¹

The aim of this report is to give an overview of optical angular manipulation of spherical LC droplets. This includes (i) the laser-trapping characteristics (i.e., the position of the droplet in the trap), (ii) the quasi-statics angular realignment, and (iii) the uniform and nonuniform rotational dynamics, for nematic, smectic and cholesteric phases. Linear elliptical and circularly polarized laser tweezers are considered, but we restrict our presentation to nonabsorbing LC droplets (which corresponds to almost all studies reported so far). Namely, all the optical effects under consideration result from a nonresonant dielectric interaction between light and LCs. This choice follows the recent work of Manzo *et al.*,³¹ who investigated in detail the influence of dye-dopants (known to resonantly enhance the optical torque^{32,33}) on the rotational dynamics of LC droplets. Indeed, Manzo *et al.* showed that the observed rigid body rotational motion (i.e., the orientational molecular order and the rotational fluid flow are locked) is not influenced in practice by the photoinduced orientational effects associated with the presence of dye molecules whereas the role of light absorption by itself is merely to change the trapping beam ellipticity threshold value above which rotation is observed.

The plan of this paper is as follows. In Sec. 2, the different kinds of LC droplets encountered in trapping experiments are presented together with the optical trapping standard setup and optical analysis tools. Before we focus on the active optical angular manipulation of droplets, their position in the optical trap as a function of their intrinsic structural order is discussed in Sec. 3, which reveals some important features associated with the elastic nature of LCs, namely light-induced elastic distortions. Then, the droplet realignment under linearly polarized tweezers is presented in Sec. 4. The transition from statics to rotational dynamics is tackled in Sec. 5. Rotational dynamics is detailed in Sec. 6, where various kinds of uniform and nonuniform rotation regimes are discussed. As a matter of fact, the orientational nonlinearities, whose manifestations are related to droplet symmetry and trapping polarization, mark out all these aspects of optical angular manipulation. Nonlinear rotational dynamics as a function of the polarization state of the trapping beam is also discussed. Finally, conclusions are drawn in Sec. 7.

2. Laser Trapping of Liquid Crystal Droplets

2.1. *The different kinds of usual droplets*

LC ordering is described by the local averaged molecular orientation given by a unit vector \mathbf{n} called the director. Here, three different LC phases are considered: nematic, cholesteric and smectic, whose description is well documented.⁸ In short, a nematic phase differs from an isotropic fluid by its structural anisotropy, which is reflected in all its macroscopic tensorial properties. In the presence of chirality, a nematic phase acquires a spontaneous torsion leading to a twisted nematic order, also called cholesteric. Finally, a smectic phase corresponds to a lamellar organization that depends on the nature of the LC building blocks, which results in many subcategories of smectic phases.⁸ Only smectic phase A, where the director is perpendicular to the lamellar planes, will be considered here due to the very small number of tweezed smectic droplets experiments reported so far.

The droplets are prepared by dispersing LCs in water, leading to self-organization into spherical microdroplets whose gross sizes are easily adjusted by mechanical stirring. Various kinds of droplets can be obtained, depending on the LC phase and the boundary conditions at the surface of the droplet. Those discussed here are shown in Fig. 1, where cases (a) and (d) refer to planar boundary conditions (i.e., the director is parallel to the surface) and cases (b) and (c) refer to homeotropic ones (i.e., the director is perpendicular to the surface). For nematic droplets [see Figs. 1(a) and 1(b)], bipolar or radial bulk ordering is obtained by addition of an appropriate surfactant. Any anionic (e.g. SDS), cationic (e.g. CTAB) or neutral (e.g. TWEEN20) surfactant can be used to change surface anchoring. This is illustrated in Fig. 1(e), where the probability for a 5CB nematic droplet to have a radial director alignment versus the concentration of the surfactant CTAB is shown.³⁴ In contrast, smectic droplets are found to have a radial structure [see Fig. 1(c)] even without the addition of a surfactant in the surrounding water.²⁴ Finally, the structure of a cholesteric droplet strongly depends on the ratio between the cholesteric pitch (the distance over which the director rotates by a full turn) and the droplet radius, even if the boundary conditions are unchanged.³⁵ Up to now, the studies on optically trapped cholesteric droplets have considered only low chirality regimes and planar boundary conditions.^{13,25} In that case the pitch is of the order of, or less than, the droplet radius and a twisted bipolar configuration is adopted, as depicted in Fig. 1(d).

In practice, the symmetry of the director field is revealed by imaging the droplets between two crossed polarizers under white light illumination (see Fig. 2). Typical images are shown in the panels (a')–(d') of Fig. 1. As expected, the radial nematic (b') and smectic (c') droplets possess identical symmetry and give a similar pattern whereas bipolar nematic (a') and twisted bipolar cholesteric (d') droplets can be independently identified. Note the remaining degeneracy between the radial nematic/smectic and the bipolar nematic droplets if the bipolar axis is parallel to the direction of illumination; however, as illustrated in Figs. 1(a), 1(a') and 1(d),

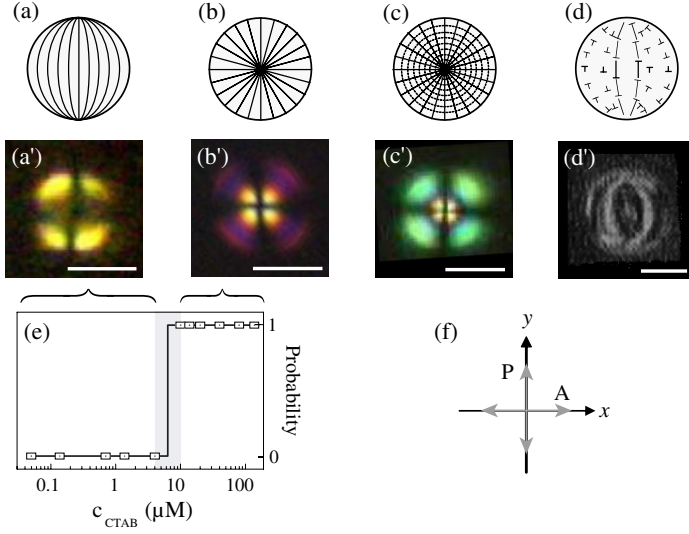


Fig. 1. Director field (x, y) cross sections and liquid crystal droplet images between crossed polarizers. (a, a') Bipolar nematic droplet; (b, b') radial nematic droplet; (c, c') smectic A nematic droplet, where the dashed lines denote the lamellar structure of the droplet ordering; (d, d') twisted bipolar long-pitch cholesteric droplet, where the cholesteric pitch is almost equal to the droplet radius (from Yang *et al.*, a shorter nail indicates that the director is pointing out of the plane of the diagram). (e) Probability of observing a radial director alignment versus the concentration of the surfactant CTAB for a 5CB nematic droplet. (f) P and A are the directions of the input polarizer and output analyzer; z is the trapping beam axis. The scale bar is $5 \mu\text{m}$.

1(d'), any bipolar axis tends to lie perpendicularly to the trapping beam propagation direction in practice. Still, bipolar and radial nematic droplet images have similar polariscopic characteristics when the bipolar axis coincides with either the P or the A direction, as illustrated in Figs. 1(a), 1(a'). However, systematic and unambiguous discrimination is readily achieved either by testing different polarizer settings or by optical trapping manipulation.

2.2. Optical trapping and polarization analysis

Laser trapping and manipulation of LC droplets generally uses continuous wave lasers at visible or near-infrared wavelength, following the setup sketched in Fig. 2. The optical trap is set with a high numerical aperture objective lens (e.g. $\text{NA} = 1.3$) whose entrance pupil is suitably fulfilled by the incoming beam through using a pair of collimation lenses (see “collimation control” box in Fig. 2). Then, for a diffraction-limited focusing, the beam spot diameter [at $\exp(-2)$ of its maximum intensity] at the focus is $\sim 1.22\lambda/\text{NA}$ and therefore of the order of the trapping beam wavelength λ . The trapping power is adjusted using a half-wave plate combined with a polarizer (see “power control” box in Fig. 2) and is obtained from the photodiode PD₁. The ellipticity angle χ and the azimuth angle ψ of the polarization ellipse of the trapping

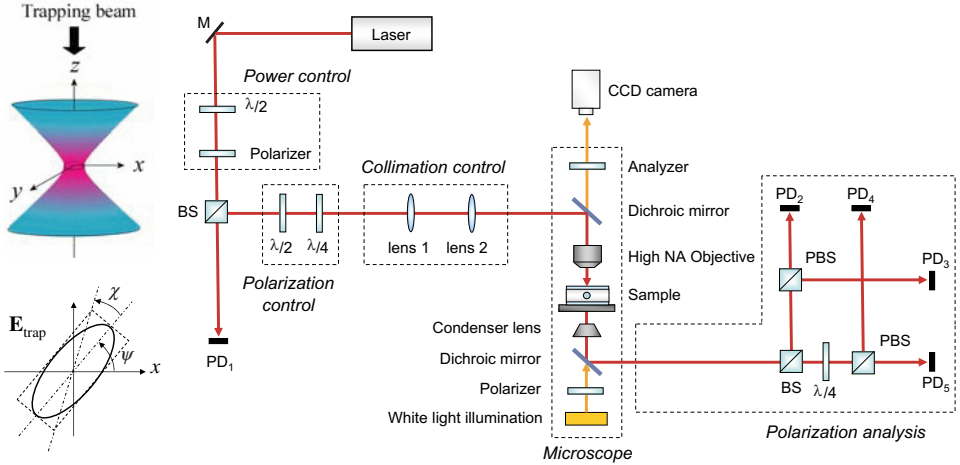


Fig. 2. Experimental setup. Left part: Trapping beam geometry and definition of the ellipticity angle χ and azimuth angle ψ of the polarization ellipse associated with the electric field \mathbf{E}_{trap} . Right part: The optical trap is obtained from a laser that is focused using a microscope objective with a large numerical aperture. M — mirror; $\lambda/2$ — half-wave plate; $\lambda/4$ — quarter-wave plate; BS — beamsplitter; PBS — polarizing beamsplitter; PD_i — photodiode.

beam (see definitions in Fig. 2) are both controlled by a pair of half- and quarter-wave plates (see “polarization control” box in Fig. 2).

The orientational structure of a trapped LC droplet is monitored both in space and analysis of the time by simultaneous crossed polarizes imaging and polarimetric trapping light at the output of the droplet (see “polarization analysis” box in Fig. 2). For this purpose, two photodiodes acquire the power of the x - and y -polarized electric field components (see $\text{PD}_{i=2,3}$ in Fig. 2), and two others the power of the left- and right-handed circularly polarized electric field components by placing a quarter-wave plate at 45° of the polarizing beam splitter main axes (see $\text{PD}_{i=4,5}$ in Fig. 2). Hence the first and third reduced Stokes parameters, $s_1 = (V_2 - V_3)/(V_2 + V_3)$ and $s_3 = (V_4 - V_5)/(V_4 + V_5)$, are obtained from the voltages values V_i detected by PD_i , which is enough to characterize the rotational dynamics of the droplets.³⁶ In practice, lenses (not shown in Fig. 2) may be placed before each of the large area photodiodes to prevent spurious aperturing effects.

2.3. Considerations on the trapping light field distribution

As we shall see later, a qualitative understanding of the behavior of a birefringent droplet in the optical tweezers may generally be obtained from simple arguments based on the crude approximation of a uniform birefringent slab interacting with a normally incident plane wave. Obviously, such consideration neglects many of the experimental features, such as the droplet spherical shape, the inhomogeneous

optical axis distribution inside the LC droplet and the tight focusing of light. Therefore, the exact nature of the light field inside the droplet is *a priori* a complicated but necessary step toward quantitative predictions of forces and torques acting on the LC. Efficient calculation methods have been developed to tackle such problems and expertise has been accumulated from the first developments made by Ashkin.^{37–40} In particular, the T-matrix method has been revealed as an efficient tool⁴³ for studying nontrivial geometries such as possibly absorbing and/or birefringent dielectric spheroids. In addition, the case of light beams that possess spin and/or orbital angular momentum, or not, have been explored in much detail.^{40–42} As a matter of fact, the case of LC droplets represent a challenging theoretical electromagnetic problem. In fact, the situation is even more tricky due to the large optical nonlinearities^{26,27} that may enrich much the force and torque densities applied on the droplet.³⁰ At least, in the present case, the typical intensity distributions of the electric field components exhibit a significant contribution only in the central part of the droplet. This is illustrated in Fig. 3, where finite domain time difference (FDTD). Calculations are shown for a calculator polarized tightly focused beam incident on a spherical uniaxial droplet having its optical axis along the beam propagation direction, which party times, for the purpose of illustration, the axial symmetry of a radial droplet.

Next, we focus, in distinct sections, on the following typical features: (i) the transverse and longitudinal positioning of a trapped droplet with respect to the trapping beam, (ii) the light-controlled angular realignment, (iii) the practical conditions for which a rotational motion takes place, and (iv) the uniform and nonuniform rotation regimes. Because these different aspects come into play simultaneously in experiments, these sections may partially overlap but hopefully emphasize the richness of the interaction of light with anisotropic fluids.

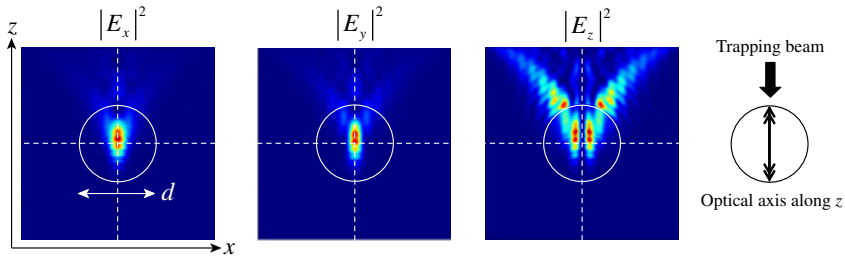


Fig. 3. FDTD calculations of the light intensity distribution $|E_{x,y,z}|^2$ in and around a dielectric nonabsorbing birefringent sphere with main refractive index $n_x = 1.5$, $n_y = 1.5$ and $n_z = 1.8$ immersed in water ($n_{\text{water}} = 1.33$) and illuminated by an incident circularly polarized Gaussian beam with wavelength $\lambda = 1064$ nm and beam waist diameter $2w_0 \simeq \lambda$ located at the origin in the absence of the sphere. The sphere is placed at the origin, and calculations are done for a sphere of diameter $d = 4 \mu\text{m}$. Only the (x, z) cross section is represented here. Note that there is roughly a factor of 30 between the maximum values of $|E_{x,y}|^2$ and $|E_z|^2$, respectively.

3. Off-Axis and Axial Positioning of a Droplet in Tweezers

It is well known that the trapping location of a spherical dielectric particle is not centered on the maximum intensity of the unperturbed incident Gaussian trapping beam, but axially displaced. This originates from refraction effects that change the hot spots' location.⁴⁰ In the case of LC droplets, a repositioning is also expected but transverse and longitudinal effects occur either separately or simultaneously, depending on the LC droplet phase and symmetry.

3.1. Nematic droplets

As a matter of fact, neither transverse nor longitudinal significant off-centering has been reported in the case of bipolar nematic droplets,^{21,22} whereas off-axis positioning is a characteristic of trapped radial nematic droplets.^{28–30} We introduce the distance ℓ between the center of the trapping beam and the droplet center of mass, as depicted in Fig. 4(a). The dependence of ℓ on tweezers ellipticity and power, which has been discussed in detail by Brasselet *et al.*,³⁰ is summarized in Figs. 4(c) and 4(d): a monotonous decrease of ℓ is observed when the polarization changes from linear ($\chi = 0$) to circular ($\chi = \pi/4$) [see panel (c)], whereas its amplitude increases with power whatever the trapping polarization is [see panel (d)].

The polarization dependence of ℓ [Fig. 4(c)] can be explained by electromagnetic free energy minimization,²⁶ which implies minimizing the volume integral of $-\epsilon_a \langle \mathbf{n} \cdot \mathbf{E} \rangle_t^2$ over the droplet (the brackets mean time averaging and ϵ_a is the anisotropy of the permittivity tensor, positive for LCs discussed here). Qualitatively, this implies a compromise between (i), the alignment of the director along the major axis of the polarization ellipse [i.e., maximization of the term $\mathbf{n} \cdot \mathbf{e}$, where \mathbf{e} is the unit vector that describe polarization state] and (ii) the droplet on-axis positioning [i.e., maximization of the light field intensity inside the droplet]. At low ellipticity values, the polarization is almost linear and the contribution (i) plays the

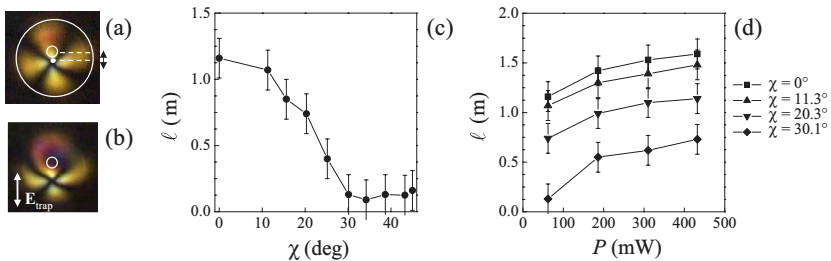


Fig. 4. Nematic droplet case. (a) Definition of the off-axis distance ℓ . The outer circle, the inner circle and the dot indicate the droplet contour, the locus of the focal spot and the droplet center of mass, respectively. Here trapping power is $P = 62$ mW, trapping polarization is linear and the droplet diameter is $d = 6 \mu\text{m}$. (b) Same as (a) for $P = 310$ mW. (c) ℓ versus ellipticity angle χ at trapping power $P = 62$ mW. (d) ℓ versus trapping power P for ellipticity angles $\chi = 0^\circ$ (squares), 11.3° (up triangles), 20.3° (down triangles) and 30.1° (diamonds).

dominant role, thus leading to a nonzero value of ℓ , whereas at large ellipticity values the polarization is almost circular and the contribution (ii) becomes prominent, which implies that $\ell \rightarrow 0$. Moreover, the power dependence [Fig. 4(d)] evidences a nonlinear effect associated with optical reordering, as shown in Fig. 4(b) for linear polarization and high trapping power. In that case, the free elastic energy associated with elastic deformations²⁶ has also to be taken into account.

The fact that $\ell = 0$ does not prevent optical reordering for circularly polarized tweezers, as shown in Fig. 5(a), where light-induced static chiral distortion is clearly evidenced from the twisted conoscopic pattern.^{28,30} Note also that the observed absence of rotation is not an artefact and is explained by the exact local compensation between the dielectric torque density and the moment of the optical radiation force density everywhere in the droplet for an on-axis droplet configuration.⁴⁴ In addition, the relationship between the optically induced chiral elastic distortions and the presence of a nonzero spin angular momentum density is confirmed by Fig. 5(b). In this figure, the twist angle β , defined in the inset of Fig. 5(a), exhibits a monotonous increase with χ (hence with the input angular momentum) and is zero for linear polarization only.

As will be discussed in more detail in the next sections, radial nematic droplets are no longer static at high power when polarization is not linear, which is a direct consequence of spin angular momentum transfer from the light to the LC. However, such rotational dynamics is associated with off-axis trapping position, as illustrated in Figs. 6(a)–6(c), where the corresponding wobbling is retrieved by following the core of the out-of-center dark cross with a fast CCD camera. In addition, the dependence of the relative wobbling amplitude on the droplet diameter shown in Fig. 6(d)

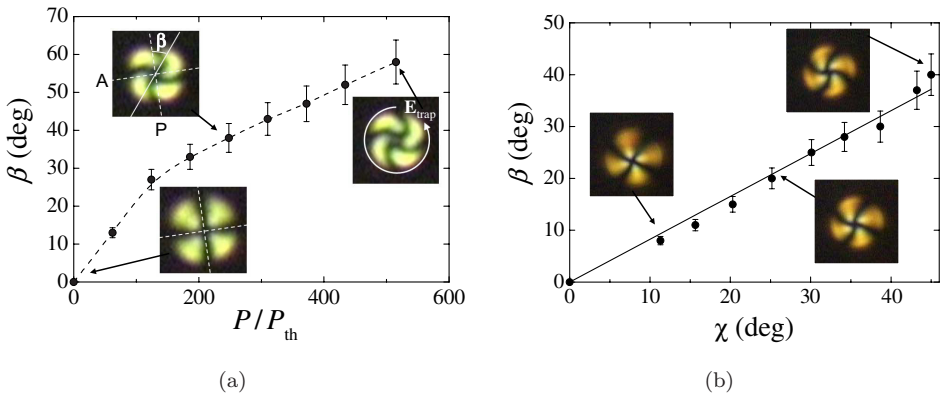


Fig. 5. (a) Power dependence of the laser-induced static twist amplitude for a 3.5- μm -diameter droplet below the rotation threshold when the trapping light field \mathbf{E}_{trap} is circularly polarized. The dashed line is guide for the eye. Insets: Illustration of the twist angle β for polariscope images of a 3.5- μm -diameter droplet, where P and A refer to the crossed analyzer and polarizer (see Fig. 2) at trapping power $P = 0, 248, 515$ mW. (b) Ellipticity dependence of the circularly polarized laser-induced static twist amplitude for a 6- μm -diameter droplet at $P = 62$ mW. The solid line is the linear fit. Insets: Images of the droplet between crossed polarizers.

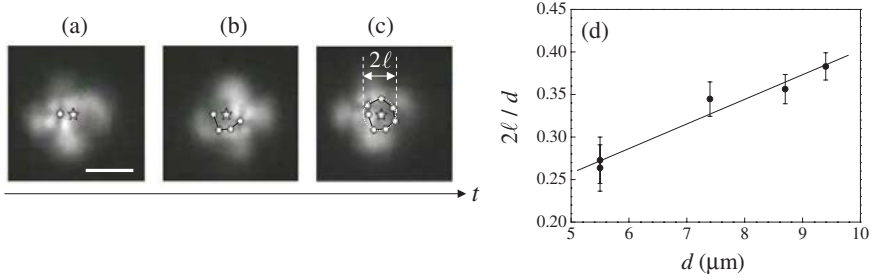


Fig. 6. (a)–(c) Crossed polarizer images of an off-axis rotating radial nematic droplet under circularly polarized tweezers at different times. Star markers indicate the trapping beam location, and the trapping power is $P = 500$ mW. The elapsed time between two snapshots is 4 ms and each of them corresponds to a circle marker. The scale bar is $5\ \mu\text{m}$, and the droplet diameter is $d = 8.7\ \mu\text{m}$. (d) Ratio between the diameter of the off-axis transverse perturbation and the droplet diameter as a function of d for $P = 500$ mW.

emphasizes a nontrivial light–matter interaction. Finally, we notice that the blurred images shown in Figs. 6(a)–6(c) are merely due to fast droplet rotation with respect to the CCD acquisition capabilities and not to axial displacement of the droplet within the trap.²⁸ In contrast, both off-axis and axial displacements may take place in smectic droplets, as discussed hereafter.

3.2. Smectic droplets

In smectic droplets, the nature of the positioning in the optical trap depends on the polarization and power of the trapping beam, and also on the droplet size. Importantly, light-induced reorientation has never been observed²⁴ although smectic droplets have the same initial ordering as the radial nematic droplet [see Figs. 1(b) and 1(c)]. The reason is to be found in the very large elastic rigidity associated with the lamellar structure of the smectic phase,⁸ which prevents the appearance of elastic light-induced distortions inside the droplet. Consequently, smectic droplets are formally free from optical reordering effects and may serve as a useful benchmark case when compared to the more complex situation of optically reoriented radial nematic droplets.

When linearly polarized tweezers are used, only static and power-independent off-axis displacement of the droplet inside the trap is unambiguously observed, in agreement with the simple compromise described in Sec. 3.1 in the absence of optical reordering. However, when the trapping beam polarization is circular, either off-axis or axial repositioning is observed, as summarized in Fig. 7, where the panel (a) indicates two distinct regions in the plane of parameters (d, P) . A transverse droplet repositioning (referred to as T) is typically observed for large diameters and low power, whereas a longitudinal one (referred to as L) is found for low diameters and large power. It is found that the T region is associated with the rotation of the droplet in a similar manner to the nematic case, as illustrated by Fig. 8, where

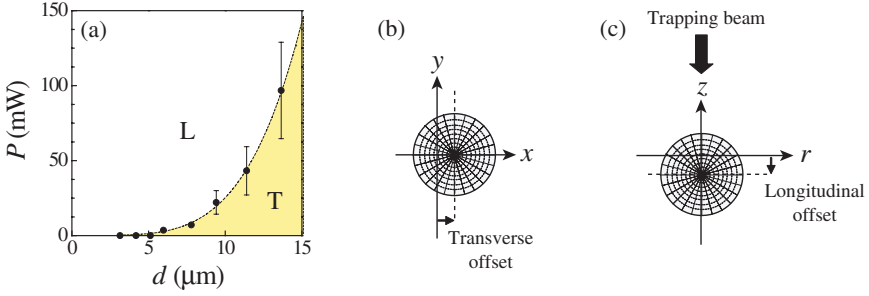


Fig. 7. Smectic droplet case. (a) Map of the trapping position in the plane of parameters (d, P) , where the T and L regions refer to transverse [see (b)] and to longitudinal off-centering [see (c)], respectively.

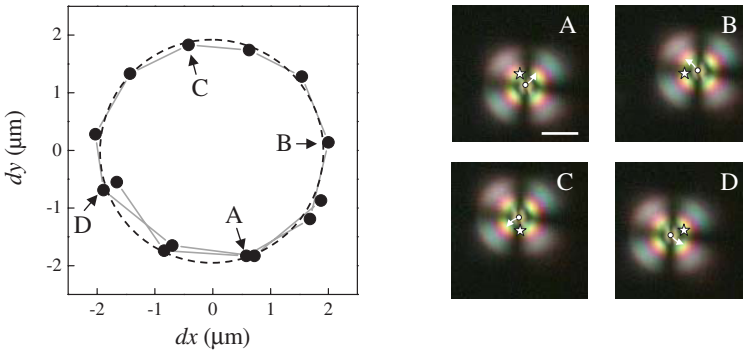


Fig. 8. Left: Off-axis wobbling trajectory of a rotating smectic droplet under circularly polarized tweezers at different times. The elapsed time between two snapshots is 33 ms, each of them corresponding to a circle marker. The dashed circle is a guide for the eye and represents a circular trajectory having a diameter of $\simeq 4 \mu\text{m}$. Right: Crossed polarizer images of the droplet at different times. The star marker indicates the trapping beam location and the trapping power is $P = 64 \text{ mW}$. The scale bar is $5 \mu\text{m}$ and the droplet diameter is $d = 10.8 \mu\text{m}$.

the wobbling trajectory of the droplet in the (x, y) plane is shown. In contrast, in the L region, which is identified by a defocusing of the droplet imaging, the on-axis droplet is not moving, in agreement with the absence of total angular momentum transfer.⁴⁴

The above-mentioned polarization effects are representative of a complex interplay between the inhomogeneous birefringent nature of the LC droplet and the incident polarization of light. To illustrate this, let us consider the off-axis configuration when trapping light is linearly polarized. Following Sec. 3.1, $|\mathbf{n} \cdot \mathbf{e}|^2 \sim 1$ in the focal region in that case. Indeed by considering the trapping position to be in the equatorial plane of the droplet, the small axial extension of the focal region of the order of λ , allows us to consider that \mathbf{n} almost lies in the (x, y) plane within the focal volume. When the polarization is circular, we have instead $|\mathbf{n} \cdot \mathbf{e}|^2 \sim 1/2$,

and the actual trapping position subsequently becomes more loose, which we believe actively participates in the $T \rightarrow L$ transition when power is increased [see Fig. 7(a)]. In addition, let us recall that an isotropic sphere in a Gaussian beam is known to be trapped on-axis but with a small longitudinal offset⁴⁰ — a feature that is expected for a radial droplet too. The last step of the reasoning is to note that an off-axis radial droplet may experience a nonzero net spin angular momentum transfer, and hence a rotational motion, which perturbs the off-axis droplet position and might irreversibly kick the droplet to the on-axis stable position where rotation and associated disturbance are absent, thus preventing any further change. We believe that this offers a realistic explanation for the sudden change of trapping position with polarization, although a fully satisfying explanation would require a quantitative analysis.

3.3. Cholesteric droplets

Twisted bipolar droplets also exhibit off-centered repositioning in an optical trap. However, in contrast to nematic or smectic LC phases, cholesteric droplets can show a periodic axial displacement for linearly polarized laser tweezers, which is actually coupled with droplet rotation²⁵ (discussed later in Sec. 5). Although the amplitude of such a vertical motion, a few tenths of microns, is a few times smaller than those observed in the transverse plane for linear [see Fig. 4(c) for $\chi = 0$] or circular [see Figs. 6 and 8] polarized tweezers, it is easily detected from blurred droplet edges when imaging is done between parallel polarizers, as shown in Fig. 9. The trapping position changes at fixed polarization and power were explained by Yang *et al.*²⁵ on the basis of periodic cycles of light-induced unwinding and rewinding of the large pitch cholesteric droplets. Such an explanation is indeed supported by theoretical investigation of the action on light on large pitch cholesteric materials,⁴⁵ where

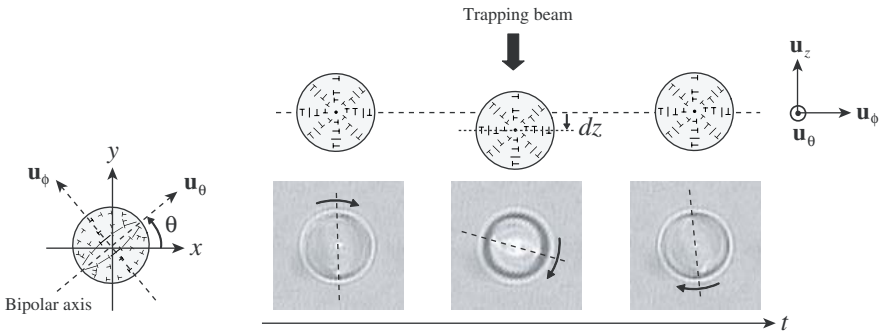


Fig. 9. Axial dynamics of a twisted bipolar cholesteric droplet under linearly polarized tweezers, from Yang *et al.* The natural pitch of the droplet is $p = 7.8 \mu\text{m}$ and the droplet diameter is $d = 8.2 \mu\text{m}$. Periodic blurring of the droplet images between parallel polarizers evidences the periodic vertical motion of the droplet. Note that the liquid crystal director configuration inside the droplet experiences time-dependent distortions that are not represented here.

optical unwinding was demonstrated to occur at light intensity values accessible to trapping experiments. Interestingly, the vertical movement toward negative values of z (see Fig. 9) approximately reached its maximum amplitude right before the helix rewinds in the droplet, i.e., when the droplet director distribution is more uniform as a result of optical unwinding. This might be connected with the axially displaced trapping position of an isotropic sphere.⁴⁰

3.4. Summary

Off-axis and/or axial repositioning of optically trapped LC droplets primarily depends on the LC phase, but the droplet inhomogeneous birefringence and optical reordering definitely enrich the picture. Either static, transient or dynamical behaviors have been identified experimentally, depending on the polarization and power of the laser tweezers. Finally, simple reasoning based on energy minimization and optical reordering brought a qualitative understanding.

4. Light-Controlled Static Angular Realignment

The angular manipulation of a sphere does not make much sense if its spherical symmetry is not broken, which naturally happens in ordered phases of LC droplets. Straightforward situations are those of bipolar nematic and twisted bipolar cholesteric droplets that possess a well-defined structural axis defined by their diametrically opposite point defects [see Figs. 1(a) and 1(d)]. However, radially ordered nematic or smectic droplets [see Figs. 1(b) and 1(c)] can also exhibit broken spherical symmetry once trapped in laser tweezers, which can be either associated, or not, with orientational nonlinearities. In this section, different possibilities to achieve optically controlled angular realignment using linearly polarized light are presented.

4.1. Nematic droplets

The orientation of on-axis trapped bipolar nematic droplets as a function of the plane of polarization of an incident linearly polarized light is shown in Fig. 10(a). In practice, the bipolar axis direction is retrieved from the droplet images between crossed polarizers.²¹ Such a behavior is a standard optical manipulation technique when one deals with uniaxial birefringent⁷ or form birefringent^{46,47} micro-objects having a well-defined overall optical axis. Less obvious is the situation where there is no direction for the averaged optical axis, as is the case for radial nematic droplets. However, an effective angular manipulation is obtained in that case too, as shown in Fig. 10(b). This is due to a radial symmetry breaking,³⁰ which is reinforced by optical realignment that tends to increase locally the effective birefringence in the focal region of the beam, as discussed in Sec. 3.1.

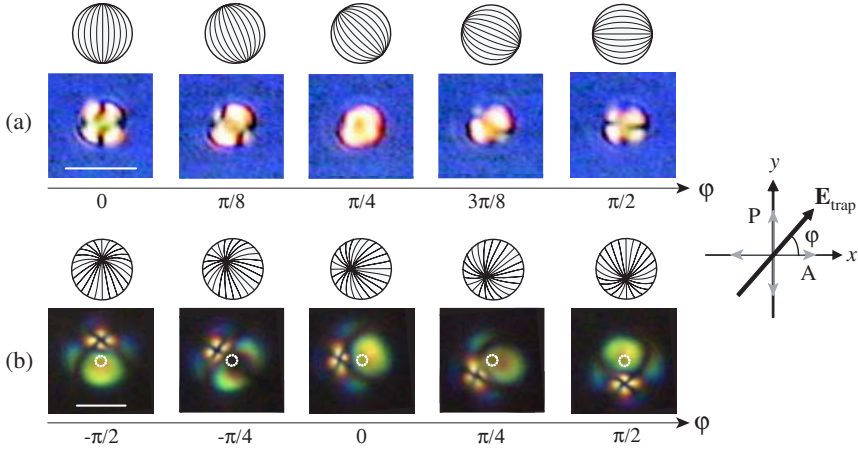


Fig. 10. Nematic droplet case. Director field cross sections in the (x, y) plane, and corresponding bipolar (a) and radial (b) nematic droplet images between crossed polarizer images as a function of the polarization plane angle φ , whose definition is given in the right part of the figure. The scale bar is $5 \mu\text{m}$.

4.2. Smectic droplets

The case of smectic droplets is similar to that of radial nematic droplets — noting, however, that the lamellar order prevents nonlinear light-induced effective birefringence changes, as depicted in Fig. 11.

4.3. Cholesteric droplets

As for bipolar nematic droplets, the bipolar axis of long-pitch cholesteric droplets trapped under linearly polarized incident light lies in the plane transverse to the beam propagation direction.^{13,25} When the laser is switched on, the droplet axis is generally observed to realign at a fixed equilibrium angle φ_{eq} with respect to the polarization direction [see Fig. 12(a)]. Further controlled rotation is achieved by rotating the incident polarization plane. However, φ_{eq} strongly depends on the droplet diameter d , as shown in Fig. 12(b), in contrast to the case of bipolar nematic droplets. In particular, abrupt variations of φ_{eq} are observed for droplets

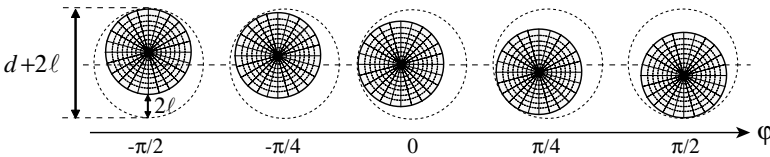


Fig. 11. Smectic droplet case. Director field cross sections in the (x, y) plane as a function of the polarization plane angle φ .

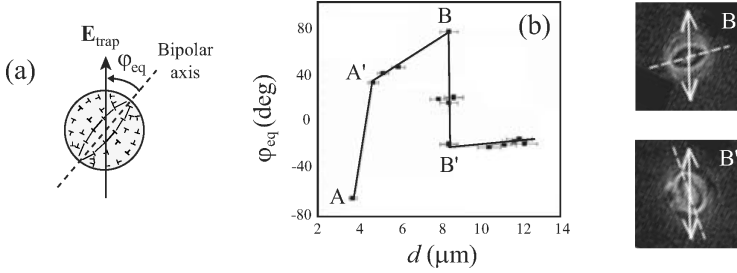


Fig. 12. Twisted bipolar cholesteric droplet case. (a) Definition of the relative orientation angle φ between the bipolar axis of the droplet (dashed line) and the trapping beam polarization direction given by \mathbf{E}_{trap} . (b) Equilibrium angle φ_{eq} (recast in the range $[-90^\circ, 90^\circ]$) as a function of the droplet diameter d , from Yang *et al.* The pairs of data (A, A') and (B, B') correspond to the droplet diameter for which an abrupt change of the droplet orientation is observed. The arrows in the insets on the right refer to the direction of \mathbf{E}_{trap} , and the dashed lines to the bipolar axis.

having diameter-to-pitch-length ratios of around 0.5 and 1, which are indicated in Fig. 12(b) by the two pairs of data (A, A') and (B, B'). This is related to the appearance of a continuous rotation of the droplet,²⁵ which will be discussed in more detail in the next section.

5. Conditions for Light-Induced Rotations

As a matter of fact, droplet rotation is obtained when light angular momentum is transferred to matter. Although it is intuitive to use a light that bears a nonzero angular momentum, this is not a compulsory requirement. Indeed, a nonzero net angular momentum transfer to an LC droplet can also be obtained with elliptically polarized or even linearly polarized trapping beams under conditions that depend on the LC phase and ordering symmetry.

5.1. Droplets with bipolar symmetry

5.1.1. Bipolar nematic droplets

Bipolar nematic droplets are a case study for angular momentum transfer through a birefringent plate behavior. To account for the actual polarization changes arising when a tightly focused beam passes through with an inhomogeneous birefringent element is, however, a nontrivial task. A zero-order approximation consists in retaining only the polarization changes experienced along the direction at the central geometrical ray, as depicted in Fig. 13(a) by a dashed arrow. The simplified problem is therefore described by a normally incident plane wave passing through a birefringent plate with thickness d and birefringence Δn_{eff} . Although crude, such an approximation is generally found in practice to offer a satisfying qualitative explanation for the main observed features, in particular the existence of the trapping

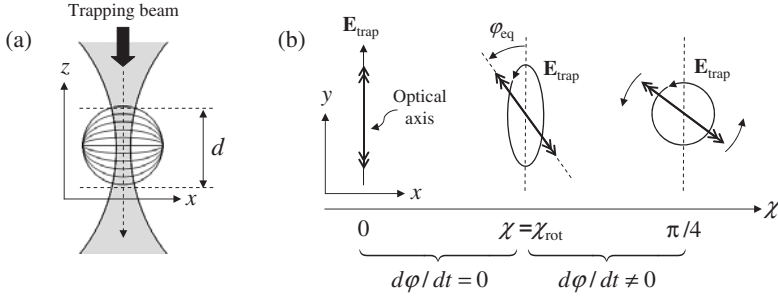


Fig. 13. (a) Ellipticity rotation threshold for a bipolar nematic droplet; the dashed arrow corresponds to the optical path retained for the calculations of the phase delay associated with the light angular momentum transfer. (b) Illustration of the trapping beam ellipticity threshold for light-induced rotation; $d\varphi/dt$ is the angular velocity of the droplet around the z axis.

beam ellipticity threshold, $\chi = \chi_{\text{rot}}$, above which a rotation settles [see Fig. 13(b)]. For this purpose we introduce the optical torque along z ,⁷

$$\Gamma_{\text{opt},z} = \left(\frac{P}{\omega}\right) [\sin 2\chi (1 - \cos \Psi) - \cos 2\chi \sin \Psi \sin 2\varphi], \quad (5.1)$$

where ω is the light angular frequency, φ is the angle between the polarization ellipse major axis [i.e., y in Fig. 13(b)] and the optical axis that lies in the (x, y) plane, and Ψ is the on-axis phase delay between the ordinary and extraordinary waves passing through the droplet. Namely, in the bipolar nematic case,

$$\Psi_{\text{bipolar}} = \frac{2\pi d \Delta n_{\text{eff}}}{\lambda}. \quad (5.2)$$

The first term of Eq. (5.1) corresponds to the spin angular momentum deposition that tends to rotate the director around the z axis. The second term is a restoring contribution due to circular symmetry breaking, when the incident polarization is not circular (i.e., $\cos 2\chi \neq 0$), which tends to align the director along the polarization ellipse major axis [see Fig. 13(b)]. For linear polarization, only the first term is zero and the equilibrium corresponds to $\varphi_{\text{eq}} = 0$. When polarization is elliptical, the competition between the two opposite contributions results in a well-defined reorientation angle, $\varphi_{\text{eq}} \neq 0$, but only if the ellipticity angle χ is not too high. The corresponding solution reads $\sin 2\varphi_{\text{eq}} = \tan 2\chi (1 - \cos \Psi_{\text{bipolar}}) / \sin \Psi_{\text{bipolar}}$ for $\chi < \chi_{\text{rot}}$, where χ_{rot} satisfies

$$\chi_{\text{rot}} = \frac{1}{2} \arctan \left[\frac{\sin(2\pi d \Delta n_{\text{eff}} / \lambda)}{1 - \cos(2\pi d \Delta n_{\text{eff}} / \lambda)} \right], \quad (5.3)$$

and above which the droplet is put into regular rotation ($d\varphi/dt = \text{const}$) or not ($d\varphi/dt \neq \text{const}$), depending on ellipticity and power, as further detailed in Sec. 6. The confrontation with experiments is illustrated in Fig. 14, where χ_{rot} is plotted as a function of the droplet diameter d for $\lambda = 1064 \text{ nm}$ ³⁴ and 785 nm .³¹ In both cases the best fit using Eq. (5.3) and Δn_{eff} as the only adjustable parameter gives almost

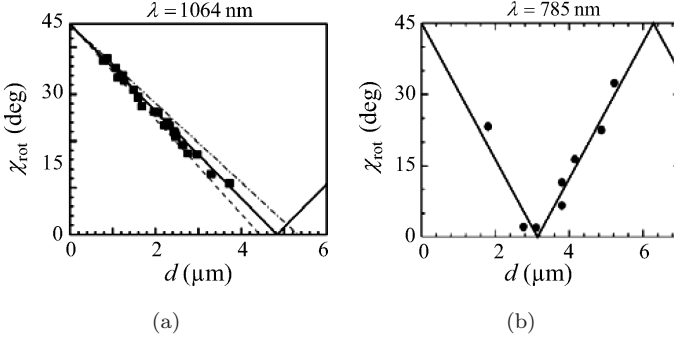


Fig. 14. Ellipticity threshold χ_{rot} vs. d of a bipolar nematic droplet at $\lambda = 1064$ nm (a) and $\lambda = 785$ nm [from (b), Manzo *et al.*]. The markers correspond to experimental data and the solid line to the best fit, the birefringence Δn being the only adjustable parameter. The dashed lines in panel (a) illustrate the robustness of the fitting procedure, with the theoretical plot obtained with $\Delta n_{\text{best fit}} \pm 0.01$.

identical results, $\Delta n_{\text{eff}} \simeq 0.11$ [case (a)] and $\Delta n_{\text{eff}} \simeq 0.12$ [case (b)], respectively. These two situations, where experimental data correspond typically to a decreasing (resp. increasing) part of the curve $\chi_{\text{rot}}(d)$, validate the dependence on d and λ of the birefringent slab approach. It could be argued that the measured Δn_{eff} is roughly twice lower than the actual birefringence of LC, $\Delta n \sim 0.2$. However, the influence of the tight focusing used in practice, which is expected to reduce the overall effective birefringence due to local oblique incidence, is completely neglected here.

Also, we note that such results are found to be LC-dependent in experiments. Indeed, the data reported in Fig. 14 correspond to nematic LC mixture E44 or E63. Interestingly, similar experiments reported using 5CB nematic exhibit a departure from the solid birefringent plate behavior, which was interpreted in terms of light-induced reordering due to lower elastic constants.³⁴ Accordingly, recent investigations of the nonlinear rotational dynamics of 5CB bipolar droplets have confirmed the presence of possible highly nonlinear behavior in that case³⁶ (see Sec. 6).

5.1.2. Cholesteric twisted bipolar droplets

As in the bipolar nematic case, cholesteric droplets of the bipolar type are put into rotation when trapped in circularly polarized tweezers,²⁵ but experimental data are not yet published. However, in stark contrast to the nematic case, rotation may also be observed for linear polarization when a diameter-to-cholesteric-pitch ratio of around 0.5 and 1 is set. This corresponds to abrupt variation of the bipolar axis orientation static equilibrium angle ϕ_{eq} , as indicated by the two pairs of data (A, A') and (B, B') in Fig. 12(b). The corresponding jumps are $\Delta\varphi^A = 97^\circ$ and $\Delta\varphi^B = -94^\circ$, and we believe that an angular jump amplitude $|\Delta\varphi|$ slightly larger than 90° is essential from the point of view of the left/right symmetry breaking required to obtain a continuous rotation through the optical unwinding/rewinding

process proposed by Yang *et al.*²⁵ Note that the handedness of the rotation remains an open question. As a matter of fact, since the rotation is due to the presence of chirality, its handedness is likely controlled by the handedness of the chiral dopant, which is to be confirmed experimentally. In addition, it would be interesting to demonstrate whether the sign of $\Delta\varphi$ does control the sense of rotation, which is likely too.

5.2. Droplets with radial symmetry

By considering only polarization changes, radially ordered LC droplets are expected to rotate under a fixed incident polarization only if they are trapped off-axis, i.e., $\ell \neq 0$ [see Fig. 15(a)], as a result of total angular momentum conservation.⁴⁴ Experimentally, radial nematic droplets are found to rotate only above an ellipticity angle threshold above which a rotation with $\ell \neq 0$ is observed.³⁴ As in the case of bipolar nematic droplets, an expression for such a threshold is derived by considering the phase delay Ψ_{radial} experienced by the central part of the trapping beam [see Fig. 15(b)],

$$\Psi_{\text{radial}} = \frac{2\pi}{\lambda} \int_{-z^*}^{z^*} \left\{ \left[\frac{\epsilon_{\parallel}\epsilon_{\perp}}{\epsilon_{\perp} + \epsilon_a \cos^2 \gamma(z)} \right]^{1/2} - \epsilon_{\perp}^{1/2} \right\} dz, \quad (5.4)$$

where $\epsilon_{\parallel, \perp}$ are the dielectric relative permittivities along and perpendicular to the director, $\gamma(z) = \arctan(\ell/z)$, $z^* = R \arcsin(\ell/R)$, with $R = d/2$ being the droplet radius.³⁰ This corresponds to a plate with thickness d and effective birefringence

$$\Delta n_{\text{eff}} = \frac{\lambda \Psi_{\text{radial}}}{2\pi d}, \quad (5.5)$$

which is used to fit the experimental data for $\chi_{\text{rot}}(d)$ from Eq. (5.3), which gives $\Delta n_{\text{eff}} \simeq 0.022 \pm 0.015$ ³⁴ [see Fig. 15(c)]. Self-consistency of the approach is tested by calculating Δn_{eff} from the off-centering length measurements $\ell_{\text{rot}}(d)$ (see Fig. 4),

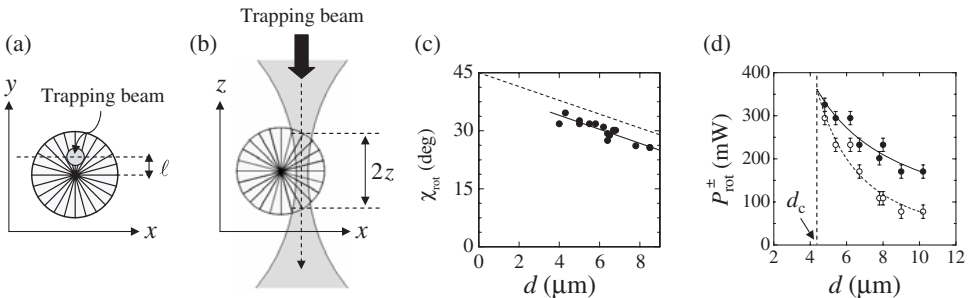


Fig. 15. (a, b) Ellipticity rotation threshold for a radial nematic droplet; the dashed arrow corresponds to the optical path chosen for the simple wave plate model. (c) The markers correspond to experimental data and the solid line is the best linear fit, and the dashed line is a same-slope extrapolation giving $\chi_{\text{rot}} = \pi/2$ at $d = 0$. (d) Droplet diameter dependence of the rotation threshold powers P_{rot}^{\pm} (open and filled markers, respectively) as defined in the text.

by solving Eqs. (5.4) and (5.5). One obtains $\Delta n_{\text{eff}}|_{\chi=\chi_{\text{rot}}} = 0.045 \pm 0.005$, which is typically twice larger than the measured value. Interestingly, such a discrepancy by a factor of 2 is similar to what is found for bipolar nematic droplets, thus emphasizing the universal character of the wave plate approach.

Radial nematic droplets under circular polarization may nevertheless lead to rotation above a threshold power at which a transition from $\ell = 0$ to $\ell \neq 0$ occurs, as shown in Fig. 15(d), where filled and open markers correspond to threshold power P_{rot}^{\pm} , respectively. While a stable rotational motion settles above P_{rot}^+ , no rotation is observed below $P = P_{\text{rot}}^-$. In between, droplets are neither continuously rotating nor immobile. Observations for various droplet diameters are summarized in Fig. 15(d). A characteristic diameter d_c below which the intermittent region vanishes, i.e., $P_{\text{rot}}^- = P_{\text{rot}}^+$, can be defined by extrapolating the data as the intersection of the power law fits [see Fig. 15(d)].³⁰

Finally, note that experimental data reported so far for smectic droplets²⁴ (i) did not evidence the existence of a rotation power threshold and (ii) did not explore polarization effects for elliptically polarized light, which we believe to be related to the absence of light-induced reordering in the smectic phase.

6. Light-Induced Rotational Dynamics

Experimentally, the angular velocity $d\varphi/dt$ of a rotating droplet is found to be a constant or not, thus corresponding to a uniform or a nonuniform (e.g. nonlinear or transient) rotation regime, respectively. As a matter of fact, the characteristics of the rotational dynamics depend on the LC droplet initial ordering, the trapping beam power and polarization.

6.1. Nematic droplets

Spinning of bipolar or radial nematic droplets is unambiguously evidenced by the rotating motion of a nearby droplet dragged by the surrounding fluid flow, as shown in Fig. 16. The use of a probe particle to map the fluid flow in a microfluidic environment is a powerful technique⁵⁰ but when the angular motion of the light-induced rotating droplet is of interest, the most reliable method consists in monitoring the polarization dynamics of the trapping light emerging from the droplet.^{23,34}

6.1.1. Influence of the trapping beam power

The power dependence of the rotation frequency f is shown in Fig. 17 for both bipolar (a) and radial (b) droplets, which exhibit qualitatively different behaviors. This illustrates how the light-induced LC distortion inside the droplet may affect the overall angular momentum transfer.

On the one hand, the linear dependence observed for bipolar droplets [Fig. 17(a)] is explained by a rigid birefringent plate behavior^{7,31} through considering the

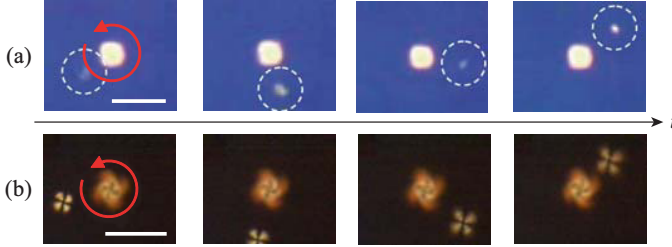


Fig. 16. Crossed polarizer images of a dragged particle in the fluid flow induced by a bipolar (a) and a radial (b) nematic droplet under circular polarization. The time elapsed between two images is 30 ms in (a) and 0.6 s in (b), which allows the visualization of the internal droplet structure. The red arrows indicate the handedness of the input circular polarization, and the scale bars are 5 μm .

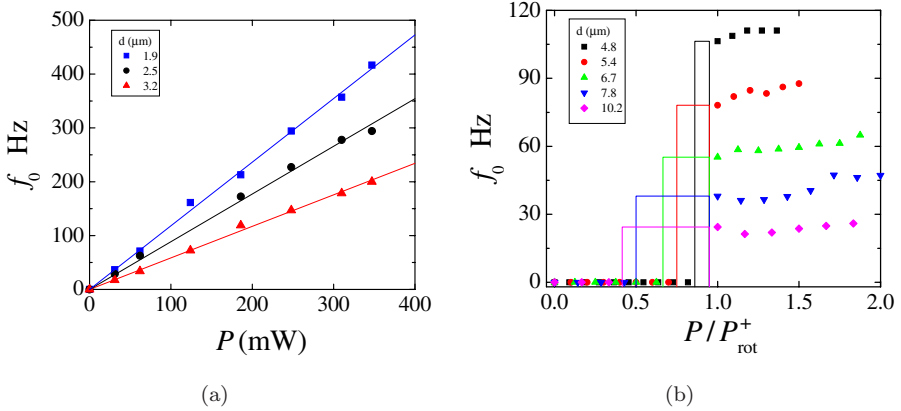


Fig. 17. Power dependence of the laser induced rotation frequency of 5CB bipolar (a) and radial (b) nematic droplets when light is circularly polarized. In case (a) the solid lines are linear fits in agreement with Eq. (6.2), and in case (b) the bars indicate the intermittent rotation region between P_{rot}^- and P_{rot}^+ ; see Fig. 15(d).

balance between the optical torque [Eq. (5.1)] and the viscous torque (Stokes law),

$$\Gamma_{\text{visc},z} = \pm 2\pi\eta\pi d^3 f, \quad (6.1)$$

where η is the dynamic viscosity of the surrounding fluid and the \pm sign accounts for the handedness of the incident polarization state of light (hence the sense of rotation around the beam axis). For circular polarization, one obtains a stationary frequency

$$f_0 = \frac{P(1 - \cos \Psi)}{2\pi^2\omega\eta d^3}. \quad (6.2)$$

The linear dependence on trapping power is well-satisfied for small droplets as shown in Fig. 17(a). For larger droplets, a more complex rotational motion is observed, as we will see later. From a practical point of view, such a linear dependence can be used to measure the viscosity of the surrounding fluid^{51,52} once the effective birefringence and the droplet diameter are known [see Eq. (5.2)].

On the other hand, the behavior of radial nematic droplet is clearly nonlinear, as shown on Fig. 17(b), with a rotation frequency almost constant above a rotation power threshold. Such a behavior can be understood from the knowledge of the light-induced director rotation in homeotropic film^{53,54} (i.e., the director is initially perpendicular to the plane of the film), since it represents a simplest 1D analog model.³⁰ In that case, there is a hysteretic rotational director dynamics related to the light-induced twisted reorientation modes, which are at the origin of an energy coupling between the ordinary and extraordinary fields during propagation of light inside the LC, as recognized by Zolot'ko and Sukhorukov.⁵⁵ This picture agrees with the crossed polarizer images of a spinning droplet shown in Fig. 16(b), where a twisted reordering pattern is clearly seen. More generally, a systematic comparison of the 1D slab analog case with angular optical manipulation of radial nematic droplets has been shown to be fruitful for obtaining a qualitative understanding of experimental observations.³⁰

A nonlinear rotational behavior is, however, not restricted to the case of radial droplets. Indeed, bipolar droplets exhibit a nonlinear rotational dynamics, as summarized in Fig. 18, where the power-dependent Fourier spectra of the first Stokes parameter of the output light are shown for droplet diameter $d = 1.4, 2.7, 7.2 \mu\text{m}$. In each case the Stokes parameters were measured for 40 successive steps with increasing power, up to 1.5 W, followed by 40 additional steps with decreasing power, as illustrated in Fig. 18(a). For a solid birefringent wave plate, one expects single-valued spectra having a linear behavior with respect to trapping power,³⁶ whose slope depends on the plate characteristics (thickness and birefringence). This is clearly not the case. For the smaller diameter [see Fig. 18(b)], the spectrum is almost single-valued for all powers but the droplet rotation frequency (which is half the peak frequency of the s_1 spectrum) exhibits a slight deviation from a linear behavior. For larger droplet diameters the s_1 spectrum is no longer single-valued and shows a nonlinear behavior with power [see Figs. 18(c) and 18(d)] that evidences a time dependent optical reordering. Qualitatively, the occurrence of nonlinear dynamics for large droplets can be understood by noting that the larger the droplet diameter, the smaller the elastic restoring torque (which scales as $\propto 1/d^2$), and more important is the ability of the optical field to induce significant distortions. Interestingly, we note that the ratio δ between the beam diameter and the droplet diameter, here $\delta \sim \lambda/d$, is $\delta = 0.7, 0.4, 0.15$ for $d = 1.4, 2.7, 7.2 \mu\text{m}$, respectively. The occurrence of complex orientational dynamics is thus qualitatively comforted with experimental^{56,57} and theoretical⁵⁴ results on LC films for which finite beam size effects have been shown to lead to complex reorientation dynamics.

6.1.2. Influence of the trapping beam polarization

In contrast to the above-discussed case of circular polarization for which the rotational motion can be nonuniform depending on the nematic droplet symmetry and size, and trapping beam power, the droplet rotation for elliptically polarized light

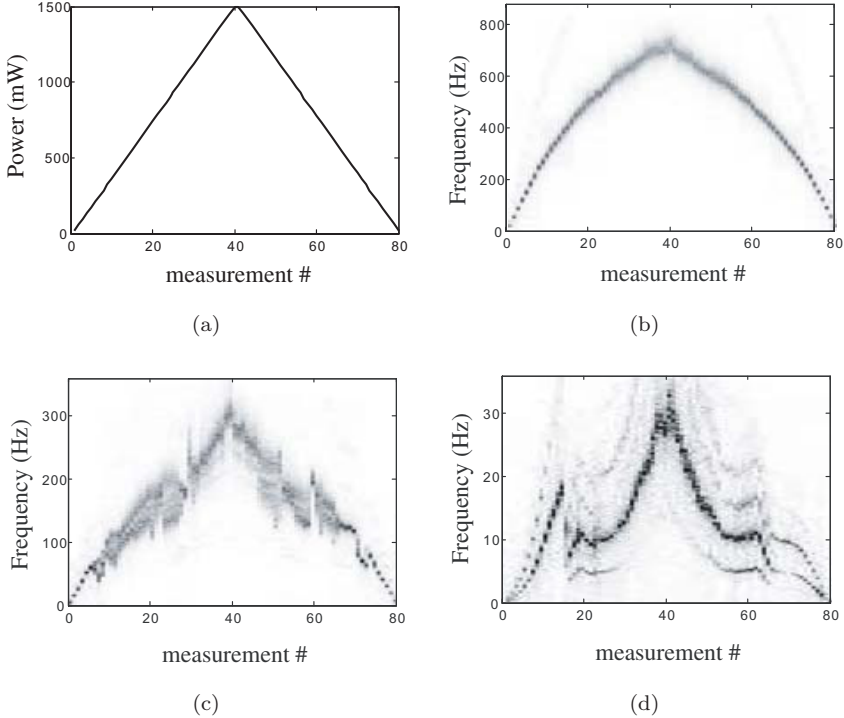


Fig. 18. (a) Optical trapping power as a function of the measurement number; (b, c, d) Fourier spectra of the s_1 Stokes parameter as a function of the measurement number for droplet diameter $d = 1.4$ (b), 2.7 (c) and $7.2 \mu\text{m}$ (d), respectively.

(which necessarily implies that $\chi > \chi_{\text{rot}}$) is in essence nonuniform as a result of the broken circular symmetry. Indeed, the second term of the optical torque in Eq. (5.1) is responsible for dynamical angular momentum exchanges, as illustrated by Fig. 19, where the spectrum of the power of output light x -polarized component is plotted for $\chi = 34.2^\circ, 36.9^\circ, 39.4^\circ, 45^\circ$. The second harmonic is clearly visible when the polarization is not circular, i.e., $\chi \neq 45^\circ$.

It is, however, possible to define the overall rotation frequency f from Eqs. (5.1) and (6.1),⁷ which is expressed as a function of χ_{rot} [see Eq. (5.3)] following

$$\frac{f}{f_0} = \sqrt{\sin^2(2\chi) - \tan^2(2\chi_{\text{rot}}) \cos^2(2\chi)}, \tag{6.3}$$

where f_0 refers to the rotation frequency for circular polarization. The normalized frequency f/f_0 versus χ is shown in Fig. 20 both for bipolar [panel (a)] and for radial [panel (b)] nematic droplets, from which we obtain satisfying agreement with the simple wave plate approach expression given by Eq. (6.3). We note, however, the presence of a hysteresis behavior in experiments that is independent of the nematic droplet structure (i.e., bipolar or radial). This recalls that although the birefringent

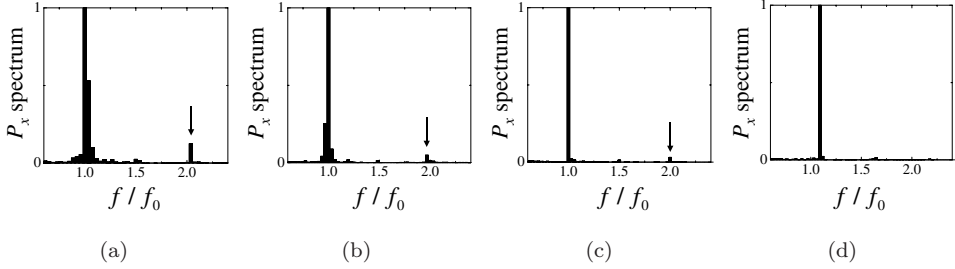


Fig. 19. Polarization dependence of the Fourier power spectra of the x -polarized output power for a $5.5\text{-}\mu\text{m}$ -diameter droplet at trapping power $P = 500\text{ mW}$, where the frequency is normalized to the fundamental frequency f_0 . Panels (a)–(d) refer to $\chi = 34.2^\circ, 36.9^\circ, 39.4^\circ, 45^\circ$, which should not be mixed up with the rotation frequency for circular polarization introduced in the text.

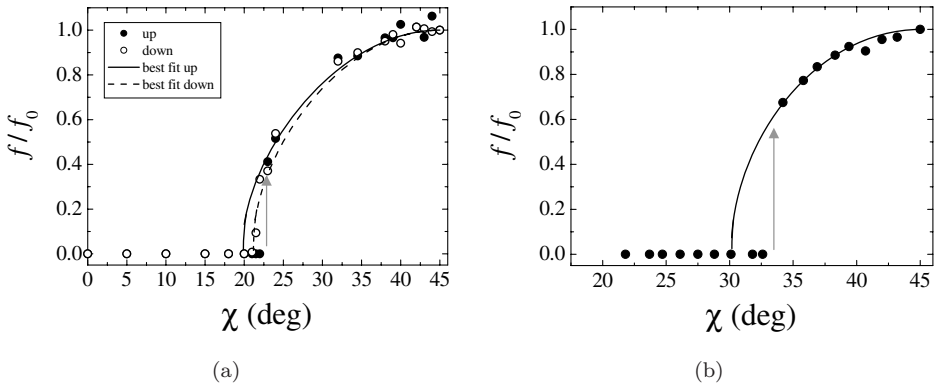


Fig. 20. Ellipticity dependence of the laser induced rotation frequency of droplets normalized to the circular polarization case, f_0 for E44 bipolar (a) and 5CB radial (b) nematic droplets with diameter $d = 2.4, 5\text{ }\mu\text{m}$, respectively. Solid lines are best fits from Eq. (6.3) but using only the rotating state data for the adjustment (i.e., $f \neq 0$) and χ_{rot} as the only fitting parameter. Gray arrows indicate when the droplet switches from the nonrotating to the rotating regime.

wave plate approach works rather well overall, it remains an approximate model that cannot encompass subtle, but reproducible, observations.

6.2. Smectic droplets

In contrast to radial nematic droplets, the rotational dynamics under circularly polarized tweezers of smectic droplets does not exhibit a power threshold²⁴ despite the same structural radial ordering. As a matter of fact, this is related to the off-axis trapping at the early stage of the observed transient dynamics (see Fig. 8) that leads to a nonzero net angular momentum transfer whatever the diameter is. Since the droplet eventually settles into a static on-axis but axially displaced trapping position (see Sec. 3.2), we introduce for convenience the pseudoperiod \tilde{T}_0 of the rotational dynamics. The power dependence of the corresponding pseudofrequency \tilde{f}_0 versus incident power is shown on Fig. 21(a) for various droplet diameters.

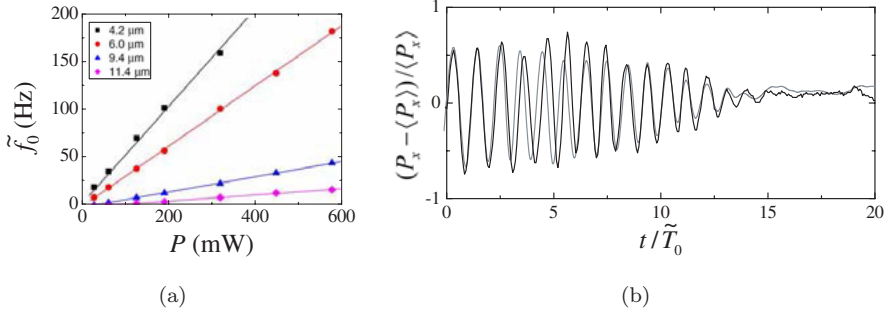


Fig. 21. (a) Rotation pseudofrequency \tilde{f}_0 as a function of trapping power for smectic droplets with different diameters. (b) Rescaled transient dynamics of the x -polarized output power P_x for droplet diameter $d = 10.8 \mu\text{m}$ and trapping power $P = 320$ mW (black curve) and $P = 576$ mW (gray curve), where \tilde{f}_0 is the pseudoperiod.

In all cases, a linear dependence is found, thus confirming the absence of optical reordering. Interestingly, the spiraling dynamics of the droplets that make a few revolutions during the descent toward the stable on-axis trapping location exhibit a roughly universal behavior as a function of power, as illustrated in Fig. 21(b), where the normalized zero-mean value of the x -polarized output power, $(P_x(t) - \langle P_x \rangle) / \langle P_x \rangle$, is plotted as a function of the reduced time t / \tilde{T}_0 for two different incident power values. In practice, such a 3D motion was proposed to determine the axial extent of the focal region of the laser tweezers.²⁴

6.3. Cholesteric droplets

As shown in Sec. 5.1.2, twisted bipolar cholesteric droplets are put into slow rotation under linearly polarized laser for a well-defined ratio between the diameter and the cholesteric pitch, $d/p \sim 0.5$ and ~ 1 . When a droplet is prepared for that specific case, the angular motion of the bipolar axis is monitored from the crossed polarizer droplet images, as shown in Fig. 22.²⁵ It is found that the rotational dynamics is strongly nonuniform, as evidenced from the time-dependent total output power of later images; see Fig. 22. Optical angular manipulation of cholesteric droplets is still in its infancy and it would not be surprising to evidence new kinds of dynamical motion related to optically induced pitch changes.

7. Conclusion and Outlook

The richness and complexity of the statics and dynamics of optical angular manipulation of a laser-trapped liquid crystal droplet has been given an overview, with a particular focus on the molecular ordering and type of the liquid crystal material. Further developments using yet-unexplored mesophases and smart liquid crystalline glassy materials whose surface could be functionalized¹⁵⁸ should be envisaged for lab-on-a-chip microfluidic devices activated by light. Indeed, optically controlled

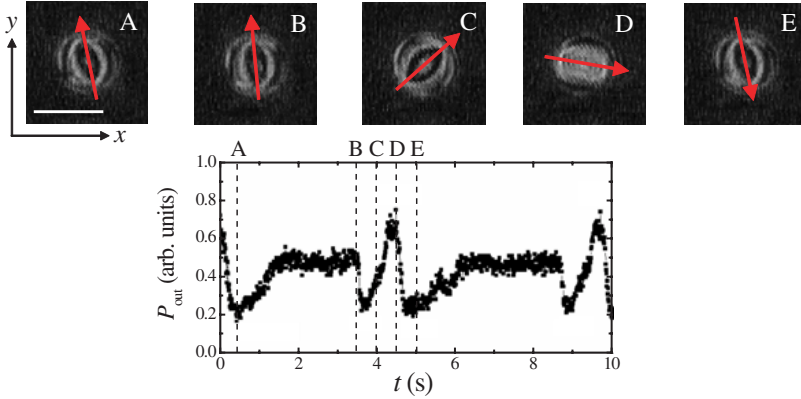


Fig. 22. Dynamics of the output power transmitted through crossed polarizers, $P_{\text{out}}(t)$, for a twisted bipolar cholesteric droplet, from Yang *et al.* The upper panels show the corresponding images of the droplet between crossed polarizers at different times. The scale bar is $10 \mu\text{m}$.

position, translation and rotation of micro/nano-objects with high spatiotemporal precision are some of the challenging issues to be addressed in order to achieve functional integrated optofluidic platforms.⁵⁹ More fundamentally, the interactions that occur at a moving interface between micro-objects and fluids at small scale are not well-understood, and optically driven and controlled birefringent microspheres of liquid crystals might be useful for this purpose. Finally, let us mention that we have focused here on the rotational dynamics of anisotropic fluids controlled by the spin part of the light angular momentum, and its extension to the orbital part of the light angular momentum is undoubtedly an interesting outlook.

Acknowledgment

We are grateful to H. Gleeson for discussions and information about laser tweezing experiments on cholesteric liquid crystal droplets.

References

1. A. Ashkin, Acceleration and trapping of particles by radiation pressure, *Phys. Rev. Lett.* **24** (1970) 156–159.
2. H. Misawa and S. Juodkazis, Photophysics and photochemistry of a laser manipulated microparticle, *Prog. Polym. Sci.* **24**(6) (1999) 65–697.
3. J. E. Molloy and M. J. Padgett, Lights, action: optical tweezers, *Contemp. Phys.* **43** (2002) 241–258.
4. D. G. Grier, A revolution in optical manipulation, *Nature* **424** (2003) 810–816.
5. D. McGloin, Optical tweezers: 20 years on, *Philos. Trans. R. Soc. A* **364** (2006) 3521–3537.
6. A. Jonáš and P. Zemánek, Light at work: the use of optical forces for particle manipulation, sorting, and analysis, *Electrophoresis* **29** (2008) 4813–4851.

7. M. E. J. Friese, T. A. Nieminen, N. R. Heckenberg and H. Rubinsztein-Dunlop, Optical alignment and spinning of laser-trapped microscopic particles, *Nature* **394** (1998) 348–350.
8. P. G. de Gennes, *The Physics of Liquid Crystals*, 2nd edn. (Clarendon Press, Oxford, 1993).
9. P. Poulin, H. Stark, T. C. Lubensky and D. A. Weitz, Novel colloidal interactions in anisotropic fluids, *Science* **275** (1997) 1770–1773.
10. I. Mušević, M. Škarabot, D. Babič, N. Osterman, I. Poberaj, V. Nazarenko and A. Nych, Laser trapping of small colloidal particles in a nematic liquid crystal: clouds and ghosts, *Phys. Rev. Lett.* **93** (2004) 187801.
11. I. I. Smalyukh, A. V. Kachynski, A. N. Kuzmin and P. N. Prasad, Laser trapping in anisotropic fluids and polarization-controlled particle dynamics, *Proc. Natl. Acad. Sci. U.S.A.* **103** (2006) 18048–18053.
12. Y. Iwashita and H. Tanaka, Optical manipulation of defects in a lyotropic lamellar phase, *Phys. Rev. Lett.* **90** (2003) 045501.
13. H. F. Gleeson, T. A. Wood and M. Dickinson, Laser manipulation in liquid crystals: an approach to microfluidics and micromachines, *Philos. Trans. R. Soc. A* **364** (2006) 2789–2805.
14. M. Yada, J. Yamamoto and H. Yokoyama, Direct observation of anisotropic interparticle forces in nematic colloids with optical tweezers, *Phys. Rev. Lett.* **92** (2004) 185501.
15. J.-I. Hotta, K. Sasaki and H. Masuhara, Manipulation of liquid crystal textures with a focused near infrared laser beam, *Appl. Phys. Lett.* **15** (1997) 2085–2087.
16. A. Pattanaporkratana, C. S. Park, J. E. Maclellan and N. A. Clark, Manipulation of disk-shaped islands on freely suspended smectic films and CDs using optical tweezers, *Ferroelectrics* **310** (2004) 131–135.
17. I. I. Smalyukh, B. I. Senyuk, S. V. Shiyonovskii, O. D. Lavrentovich, A. N. Kuzmin, A. V. Kachynski and P. N. Prasad, Optical trapping, manipulation, and 3D imaging of disclinations in liquid crystals and measurement of their line tension, *Mol. Cryst. Liq. Cryst.* **450** (2006) 79–95.
18. I. I. Smalyukh, D. S. Kaputa, A. V. Kachynski, A. N. Kuzmin and P. N. Prasad, Optical trapping of director structures and defects in liquid crystals using laser tweezers, *Opt. Express* **15** (2007) 4359–4371.
19. T. G. Mason and J. Bibette, Emulsification in viscoelastic media, *Phys. Rev. Lett.* **77** (1996) 3481–3484.
20. A. Fernandez-Nieves, G. Cristobal, V. Garces-Chavez, G. C. Spalding, K. Dholakia and D. A. Weitz, Optically anisotropic colloids of controllable shape, *Adv. Mater.* **17**(6) (2005) 680–684.
21. S. Juodkazis, M. Shikata, T. Takahashi, S. Matuso and H. Misawa, Fast optical switching by a laser-manipulated microdroplet of liquid crystal, *Appl. Phys. Lett.* **74** (1999) 3627–3629.
22. S. Juodkazis, S. Matuso, N. Murazawa, I. Hasegawa and H. Misawa, High-efficiency optical transfer of torque to a nematic liquid crystal droplet, *Appl. Phys. Lett.* **82** (2003) 4657–4659.
23. T. A. Wood, H. F. Gleeson, M. R. Dickinson and A. J. Wright, Mechanisms of optical angular momentum transfer to nematic liquid crystalline droplets, *Appl. Phys. Lett.* **84** (2004) 4292–4294.
24. N. Murazawa, S. Juodkazis and H. Misawa, Laser-manipulation of a smectic liquid crystal droplet, *Eur. Phys. J. E* **20** (2006) 435–439.

25. Y. Yang, P. D. Brimicombe, N. W. Roberts, M. R. Dickinson, M. Osipov and H. F. Gleeson, Continuously rotating chiral liquid crystal droplets in a linearly polarized laser trap, *Opt. Express* **16** (2008) 6877–6882.
26. N. V. Tabiryan, A. V. Sukhov and B. Ya. Zel'dovich, The orientational optical non-linearity of liquid crystals, *Mol. Cryst. Liq. Cryst.* **136** (1986) 1–139.
27. I. C. Khoo, Nonlinear optics of liquid crystalline materials *Phys. Rep.* **471**(5–6) (2009) 221–267.
28. N. Murazawa, S. Juodkazis, S. Matuso and H. Misawa, Control of the molecular alignment inside liquid crystal droplets by use of laser tweezers, *Small* **1** (2005) 656–661.
29. N. Murazawa, S. Juodkazis and H. Misawa, Laser manipulation based on a light-induced molecular reordering, *Opt. Express* **14** (2006) 2481–2486.
30. E. Brasselet, N. Murazawa, S. Juodkazis and H. Misawa, *Phys. Rev. E* **77** (2008) 041704.
31. C. Manzo, D. Paparo, L. Marrucci and I. Jánossy, Light-induced rotation of dye-doped liquid crystal droplets, *Phys. Rev. E* **73** (2006) 051707.
32. I. Jánossy, A. D. Lloyd and B. S. Wherrett, Anomalous optical Fréedericksz transition in an absorbing liquid crystal, *Mol. Cryst. Liq. Cryst.* **179** (1990) 1–12.
33. I. Jánossy and T. Kosa, Influence of anthraquinone dyes on optical reorientation of nematic liquid crystals, *Opt. Lett.* **17** (1992) 1183–1185.
34. N. Murazawa, S. Juodkazis and H. Misawa, Characterization of bipolar and radial nematic liquid crystal droplets using laser-tweezers, *J. Phys. D* **38** (2005) 2923–2927.
35. F. Xu and P. P. Crooker, Chiral nematic droplets with parallel surface anchoring, *Phys. Rev. E* **56** (1997) 6853–6860.
36. E. Brasselet, T. Balčiūnas, N. Murazawa, S. Juodkazis and H. Misawa, Light-induced nonlinear rotations of nematic liquid crystal droplets trapped in laser tweezers, *Mol. Cryst. Liq. Cryst.*, in press.
37. J. P. Barton, D. R. Alexander and S. A. Schaub, Theoretical determination of net radiation force and torque for a spherical particle illuminated by a focused laser beam, *J. Appl. Phys.* **66** (1989) 4594–4602.
38. K. Ren, G. Grehan and G. Gouesbet, Radiation pressure forces exerted on a particle arbitrarily located in a Gaussian beam by using the generalized Lorenz–Mie theory, and associated resonance effects, *Opt. Commun.* **108** (1994) 343–354.
39. T. A. Nieminen, H. Rubinsztein-Dunlop, N. R. Heckenberg and A. I. Bishop, Numerical modelling of optical trapping, *Comput. Phys. Commun.* **142** (2001) 468–471.
40. S. H. Simpson and S. Hanna, Optical trapping of spheroidal particles in Gaussian beams, *J. Opt. Soc. Am. A* **24** (2007) 430–443.
41. S. H. Simpson and S. Hanna, Rotation of absorbing spheres in Laguerre Gaussian beams, *J. Opt. Soc. Am. A* **26** (2009) 173–183.
42. S. H. Simpson and S. Hanna, Optical angular momentum transfer by Laguerre Gaussian beams, *J. Opt. Soc. Am. A* **26** (2009) 625–638.
43. M. I. Mishchenko, L. D. Travis and A. A. Lacis, *Scattering, Absorption and Emission of Light by Small Particles* (Cambridge University Press, 2002).
44. I. Jánossy, Electromagnetic torque and force in axially symmetric liquid crystal droplets, *Opt. Lett.* **33** (2008) 2371–2373.
45. E. Brasselet, D. O. Krimer and L. Kramer, Light-induced instabilities driven by competing helical patterns in long-pitch cholesterics, *Eur. Phys. J. E* **17** (2005) 403–411.
46. E. Santamato, A. Sasso, B. Piccirillo and A. Vella, Optical angular momentum transfer to transparent isotropic particles using laser beam carrying zero average angular momentum, *Opt. Express* **10** (2002) 871–878.

47. A. I. Bishop, T. A. Nieminen, N. R. Heckenberg and H. Rubinsztein-Dunlop, Optical application and measurement of torque on microparticles of isotropic nonabsorbing material, *Phys. Rev. A* **68** (2003) 033802.
48. R. Dasgupta and P. K. Gupta, Rotation of transparent, non-birefringent objects by transfer of the spin angular momentum of light, *Opt. Lett.* **30** (2005) 394–396.
49. A. Yu. Savchenko, N. V. Tabiryana and B. Ya. Zel'dovich, Transfer of momentum and torque from a light beam to a liquid, *Phys. Rev. E* **56** (1997) 4773–4779.
50. R. Di Leonardo, J. Leach, H. Mushfique, J. M. Cooper, G. Ruocco and M. J. Padgett, Multipoint holographic optical velocimetry in microfluidic systems, *Phys. Rev. Lett.* **96** (2006) 134502.
51. N. Murazawa, S. Juodkazis, V. Jarutis, Y. Tanamura and H. Misawa, Viscosity measurement using a rotating laser-trapped microsphere of liquid crystal, *Europhys. Lett.* **73** (2006) 800–805.
52. N. Murazawa, S. Juodkazis, Y. Tanamura and H. Misawa, Rheology measurement at liquid-crystal water interface using laser tweezers, *Jpn. J. Appl. Phys.* **45** (2006) 977–982.
53. E. Brasselet, T. V. Galstian, L. J. Dubé, D. O. Krimer and L. Kramer, Bifurcation analysis of optically induced dynamics in nematic liquid crystals: circular polarization at normal incidence, *J. Opt. Soc. Am. B* **22** (2005) 1671–1680.
54. E. Brasselet, B. Piccirillo and E. Santamato, Three-dimensional model for light-induced chaotic rotations in liquid crystals under spin and orbital angular momentum transfer processes, *Phys. Rev. E* **78** (2008) 031703.
55. A. S. Zolotko and A. P. Sukhorukov, Fréedericksz transition induced in nematic liquid crystal by circularly polarized light wave, *Pis'ma Zh. Eksp. Teor. Fiz* **52** (1990) 707–710 [*JETP Lett.* **52** (1990) 62–65].
56. A. Vella, A. Setaro, B. Piccirillo and E. Santamato, On–off intermittency in chaotic rotation induced in liquid crystals by competition between spin and orbital angular momentum of light, *Phys. Rev. E* **67** (2003) 051704.
57. E. Brasselet and L. J. Dubé, Light-induced chaotic rotations in nematic liquid crystals, *Phys. Rev. E* **73** (2006) 021704.
58. V. A. Mallia and N. Tamaoki, Design of chiral dimesogens containing cholesteryl groups; formation of new molecular organizations and their application to molecular photonics, *Chem Soc. Rev.* **33**(2) (2004) 76–84.
59. C. Monat, P. Domachuk and B. J. Eggleton, Integrated optofluidics: a new river of light, *Nat. Photon.* **1** (2007) 106–114.